Simulation of Density-Driven Frictional Downslope Flow in *Z*-Coordinate Ocean Models

MICHAEL WINTON

Geophysical Fluid Dynamics Laboratory/NOAA, Princeton University, Princeton, New Jersey

ROBERT HALLBERG AND ANAND GNANADESIKAN

Atmospheric and Oceanic Sciences Program, Princeton University, Princeton, New Jersey

(Manuscript received 4 June 1997, in final form 9 January 1998)

ABSTRACT

An important component of the ocean's thermohaline circulation is the sinking of dense water from continental shelves to abyssal depths. Such downslope flow is thought to be a consequence of bottom stress retarding the alongslope flow of density-driven plumes. In this paper the authors explore the potential for explicitly simulating this simple mechanism in *z*-coordinate models. A series of experiments are performed using a twin density-coordinate model simulation as a standard of comparison. The adiabatic nature of the experiments and the importance of bottom slope make it more likely that the density-coordinate model will faithfully reproduce the solution. The difficulty of maintaining the density signal as the plume descends the slope is found to be the main impediment to accurate simulation in the *z*-coordinate model. The results of process experiments suggest that the model solutions will converge when the *z*-coordinate model has sufficient vertical resolution to resolve the bottom viscous layer and horizontal grid spacing equal to its vertical grid spacing divided by the maximum slope. When this criterion is met it is shown that the *z*-coordinate model converges to an analytical solution for a simple two-dimensional flow.

1. Introduction

Most of the deep water in the World Ocean enters the abyss by descending along continental slopes in thin (approximately 100 m) density-driven plumes. This process is important for determining the temperature and salinity makeup of deep waters and hence their neutral levels. Price and Baringer (1994) review the properties of four such plumes: the Mediterranean to Atlantic outflow, the outflows from the Nordic seas into the Atlantic east and west of Iceland, and the Weddell Sea outflow. Their simple streamtube model (which includes Froude-number-dependent entrainment and Ekman-number-dependent broadening parameterizations) successfully reproduces some observed features of these plumes: temperatures, salinities, plume dimensions, and flow speeds. They characterize the flows as geostrophic with bottom stress allowing descent and with significant entrainment occurring some tens of kilometers downstream of the first encounter with steep topography.

Producing deep waters with the correct properties is difficult for the class of global ocean models currently being used for climate studies (Hirst and McDougall 1996). These models typically evolve to a steady state with deep water that is too warm and fresh. A possibly related problem is the inability of these models to maintain production of North Atlantic Deep Water when initialized with observed hydrography and forced with observed winds and restoring of surface temperatures and salinities to observed values (Toggweiler 1994). These problems need to be overcome in order to fully assimilate ocean data into deep-water-simulating climate models.

Parameterizations have been proposed to correct the model biases (Danabasoglu et al. 1994). A logical preliminary to this endeavor is to assess the capability of these models to explicitly simulate the key processes involved in deep-water formation and spreading. In this paper we propose to make this assessment for the plume stage of the spreading as described by Price and Baringer. This stage is especially challenging for the models because 1) the plumes are no longer in contact with the surface where their properties can be corrected by surface boundary conditions and 2) the plumes descend along slopes that are represented as a series of steps in these *z*-coordinate models (hereafter, we use the term "*z* model").

In order to make this assessment, a standard of com-

Corresponding author address: Dr. Michael Winton, GFDL/NOAA, P.O. Box 308, Princeton, NJ 08542.
E-mail: mw@gfdl.gov

parison is needed. The density-driven plume problem is too difficult for comprehensive analytical solution. Instead, we will perform twin experiments with a density-coordinate model (''ρ model'' hereafter). This kind of model is expected to perform better than the z model by virtue of 1) being more capable of maintaining water mass properties in the important adiabatic part of the flow and 2) having a better (smoother) representation of the bottom topography. For the purpose of using the density-coordinate model as a standard we have chosen to neglect entrainment of ambient water into the plumes, stratification within the ambient water, and nonlinearity in the equation of state. All three of these have been shown to be important in determining the characteristics of actual plumes (Price and Baringer 1994). Because of the absence of entrainment and our use of large density differences, our experiments are biased to favor strong sinking.

Section 2 presents the models that we shall use for the experiments. In section 3, the model simulations of the sinking of dense water from shelf to abyss are compared. This comparison reveals a large difference between the models: the rate of dense water sinking is much larger in the ρ model than in the z model. This appears to be the result of convective mixing near the bottom in the z-model solution. In section 4, we investigate the effect of convective entrainment upon two density signals as they propagate downslope in a two-dimensional (depth/offshore) z model: First, a weak signal driven downslope by wind and, second, a stronger self-advecting signal. The resolution needed to mitigate the damaging effects of convective entrainment is determined from these experiments. In section 5, we verify that the sinking rate obtained when adequate resolution is employed in this two-dimensional model agrees with a theoretical estimate and the sinking rate obtained in a comparable ρ model. The results are summarized and discussed in section six.

2. The models

In this section we present details of the two models that are common to the experiments of the next three sections. Two primitive equation models are employed in these experiments. The z model is the Geophysical Fluid Dynamics Laboratory MOM 2 Model. For details we direct the reader to Pacanowski (1995). This model has been configured with a flux-corrected transport (FCT) tracer advection scheme. The advantage of this scheme is that no explicit tracer diffusion is needed to maintain numerical stability. Although the FCT scheme itself is potentially diffusive, the combination of FCT advection without explicit diffusion has been found to be overall less diffusive than centered advection along with sufficient explicit diffusion to damp the computational mode (Gerdes and Koberle 1995). The experiments of this study are run without tracer diffusion in the z model and without layer thickness diffusion in the ρ model. Both models neglect salinity. In the z model the equation of state has been linearized to

$$\rho(T) = -\alpha T. \tag{1}$$

The thermal expansion coefficient, α, is 2×10^{-4} kg $(m^3\ °C)^{-1}$ except in the ''quasi passive'' temperature experiment of section 4 where it is 2×10^{-6} kg $(m^3\ °C)^{-1}$.

The second model is an isopycnal model (HIM), configured here with two isopycnal layers. Aside from the vertical coordinate used, two differences between the models are worth noting: 1) HIM uses a C grid whereas MOM uses a B grid and 2) HIM has a free surface, which is time stepped with a split explicit scheme (Hallberg 1997, submitted to *J. Comput. Phys.*), whereas MOM uses a rigid lid. For the purpose of this study the main feature that distinguishes HIM from the widely used MICOM isopycnal model (Bleck and Smith 1990) is its treatment of spurious downslope accelerations associated with massless layers on slopes. In HIM these are eliminated with a second-order accurate upwind-biased vertical viscosity rather than by extrapolation of pressure gradients from the interior. A more complete description of HIM can be found in Hallberg (1995).

Both models employ a Fickian vertical viscosity. When one-half the thickness of the bottom layer of the ρ model or the bottom grid cell of the z model exceeds an Ekman layer thickness ($\sqrt{2A/f}$, where A is the vertical viscosity and f is the Coriolis parameter), the bottom stress is calculated based upon a shear layer one Ekman layer thick. The horizontal viscosity in the z model and the isopycnal viscosity in the ρ model are biharmonic. Unless otherwise noted, the biharmonic coefficients are $A_h = -1 \times 10^{10}$ m^4 s^{-1} for the z model and $A_i = -1.2 \times 10^{12}$ m^4 s^{-1} for the ρ model. The z model coefficient has been set small enough so that the horizontal stress at the bottom due to the no-slip boundary condition there is negligible relative to bottom stress. The larger coefficient of the ρ-model was necessary to maintain numerical stability. Since the lateral boundary conditions are only applied at the perimeter of the basin in the ρ model, the larger lateral friction does not compete with bottom stress.

To simplify the interpretation of the results, both models are cast on a Cartesian f plane with $f = 2\Omega \sin 60°$. This is justified by the slow speeds of planetary waves in a weakly stratified high-latitude ocean, about 1 cm s^{-1} for typical parameters used in this study. The flow velocities in the experiments are typically one to two orders of magnitude larger.

3. Sinking from shelf to abyss in the two models

Our purpose now is to assess the ability of the z model to transport dense water from shelf to abyss in a frictional bottom layer as indicated by observations of the real ocean. The basin depicted in Fig. 1 is used to pro-

vide an adequate reservoir of dense fluid on the shelf, a deep place to sink, and a realistic slope between the two. North of 70°N the basin is 500 m deep. South of that latitude its depth (in meters) is

$$d = 500 + 3000\left\{1 - \exp\left[-\left(\frac{y - 60}{2}\right)^2\right]\right\} \times\left\{1 - \exp\left[-\left(\frac{y - 70}{2}\right)^2\right]\right\}\left\{1 - \exp\left[-\left(\frac{x}{4}\right)^2\right]\right\} \times \left\{1 - \exp\left[-\left(\frac{x - 20}{4}\right)^2\right]\right\} \quad (2)$$

where x is in degrees longitude at 60° and y is in degrees latititude. This formula gives a maximum slope of about 0.01, which is typical for actual continental slopes.

The horizontal resolution in both models is 0.2° lat (0.4° long at 60°). The vertical grid spacing in the z model is 70 m. The models are initialized with water over the shelf north of 70°N having 1 kg m^{-3} (=5°C in the z model) greater density than the water to the south. Both water masses are unstratified. From this initial condition the experiments evolve freely without any external forcing.

Figure 2 shows the horizontal spreading of the density signal after one year of integration. The thickness of the bottom layer is plotted for the ρ model. As will be apparent shortly, the z model evolves substantially away from a two-layer system over this period. Consequently, bottom temperature is plotted for this model rather than layer thickness based upon an intermediate temperature. In the ρ model, a Kelvin-wave-like signal propagates rapidly southward along the western boundary and northward along the eastern boundary away from the interface between the dense and light water. The dense signal reaches the southern boundary in just 30 days. In the z model the dense signal traverses this edge in about one-half year and only half of the original density contrast remains at the front. Unlike the ρ-model front, the z-model signal propagates more rapidly along the slope than at the side boundary. We have reproduced the fast propagating Kelvin-wave-like front in a version of the z model with increased offshore resolution along the western boundary. Whether the difference in the resolution needed to simulate this front arises from the different vertical coordinates or the different horizontal grid or some other reason is not currently known.

There is also a significant difference between the

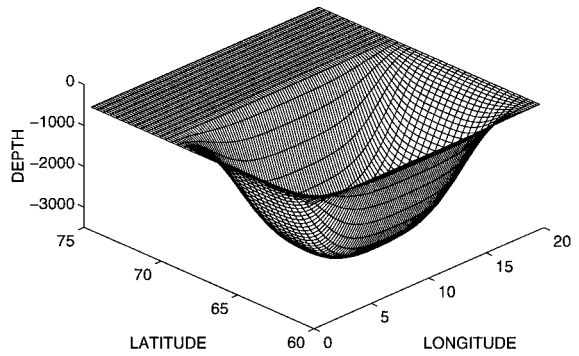

FIG. 1. Bottom topography used in the experiment of section three. The models are initialized with two homogenous water masses. The one on the shelf north of 70°N is 1 kg m^{-3} denser than the one to the south ($g' \approx 0.01$ m s^{-2}).

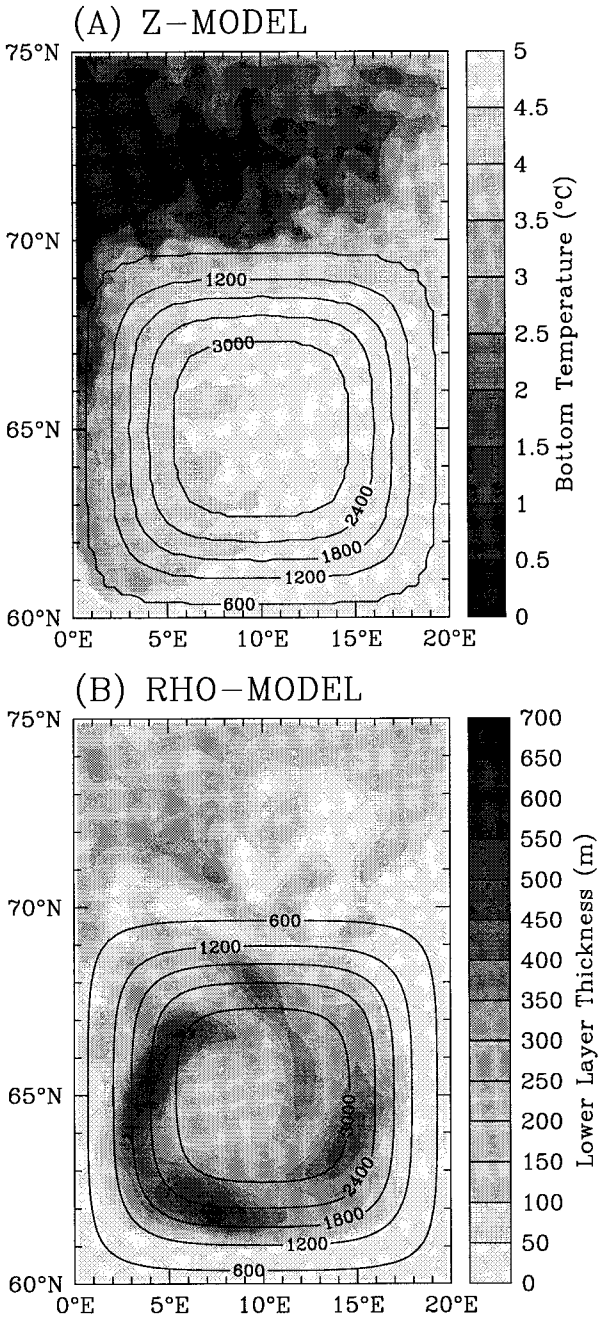

FIG. 2. Horizontal sections after the first year of (a) z-model bottom temperature (initially 0°C to the north of 70°N and 5°C to the south) and (b) ρ-model lower-layer thickness (initially zero south of 70°N).

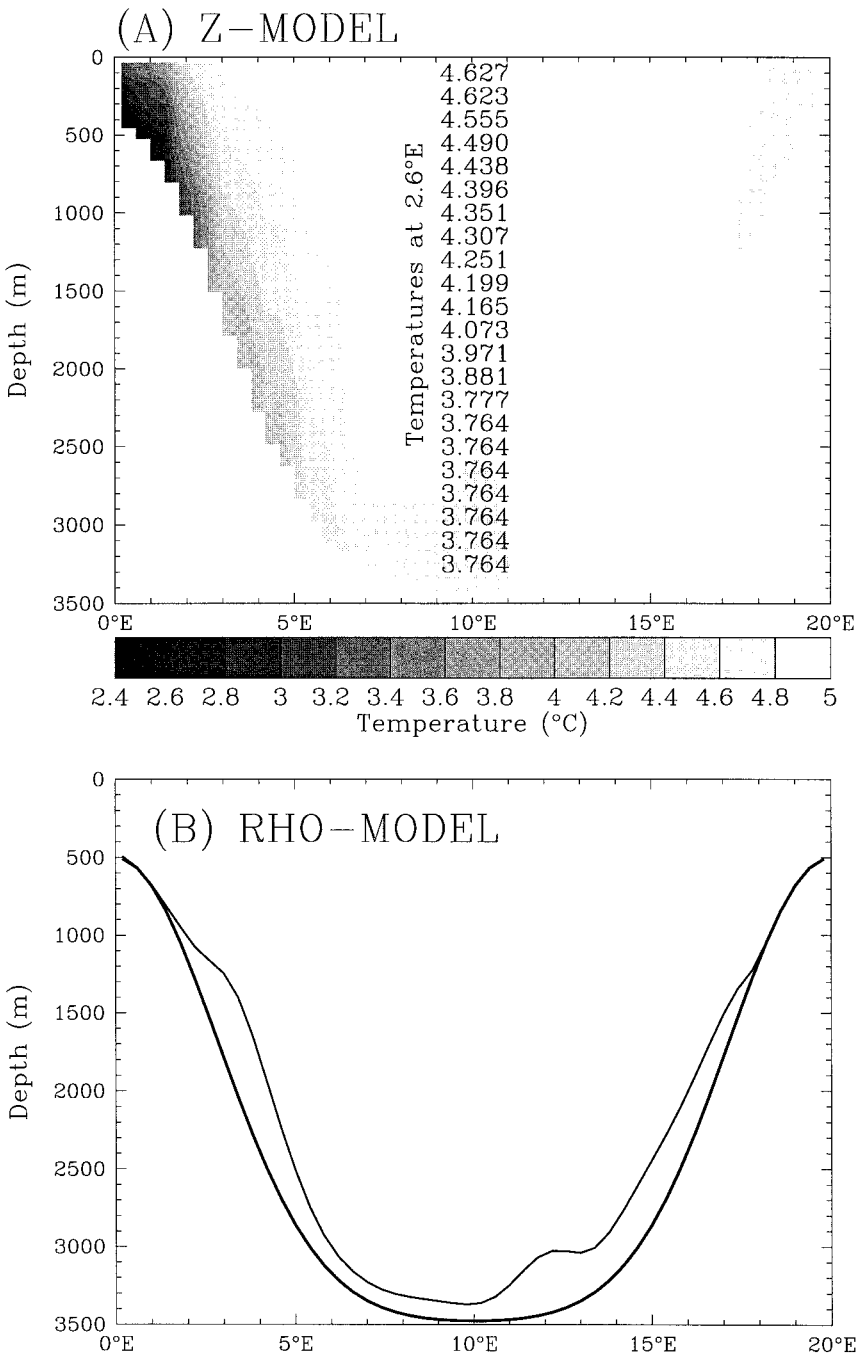

FIG. 3. Zonal sections at 65°N after 1 yr: (a) *z*-model temperature and (b) ρ-model interface. Panel a is overprinted with each of the temperatures of the 70-m-thick grid boxes at 2.6°E.

cross-slope distribution of dense water in the two models. Away from the shelf, the *z*-model bottom temperature is aligned along depth contours with cold temperatures in *shallow* regions. By contrast, the ρ model retains practically no dense water over the shallow regions on the perimeter of the bowl. In the *z* model, much less dense water has descended the slope. Figure 3 shows cross sections at 65°N at the end of 360 days of integration. Very little dense fluid can be found above 1-km depth in the ρ model, whereas there is very little cold water below this depth in the *z* model. In the *z* model, the densest water is at the top of the slope. Even there, only one-half of the original density signal remains (this water is 2.5°C warmer than the water initially placed north of 70°N). The density signal is further diminished moving offshore. Thick convective bound-

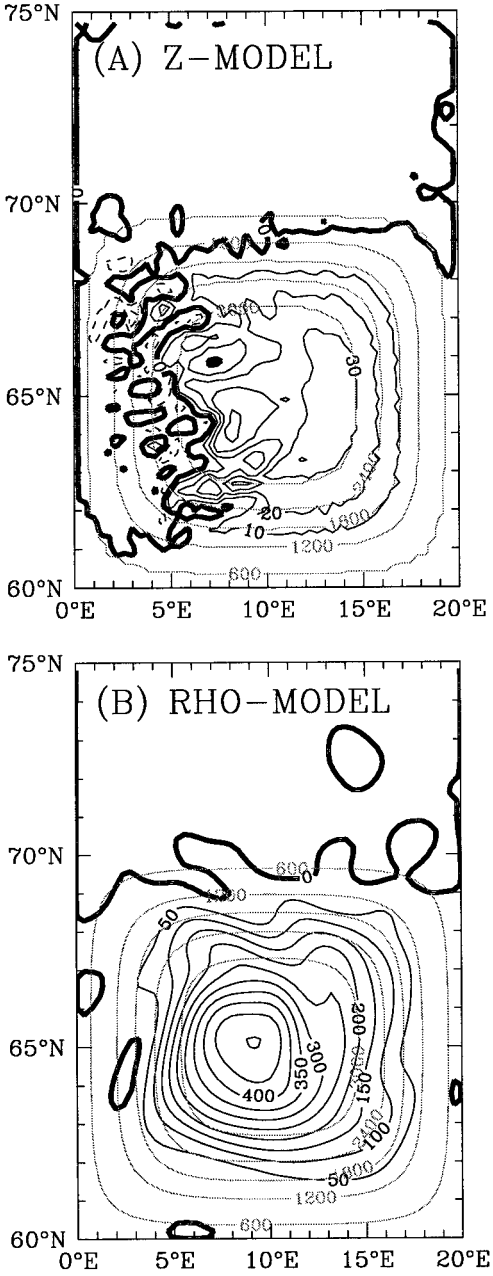

FIG. 4. Vertically integrated circulation (10^6 m^3 s^{-1}) after 1 yr.

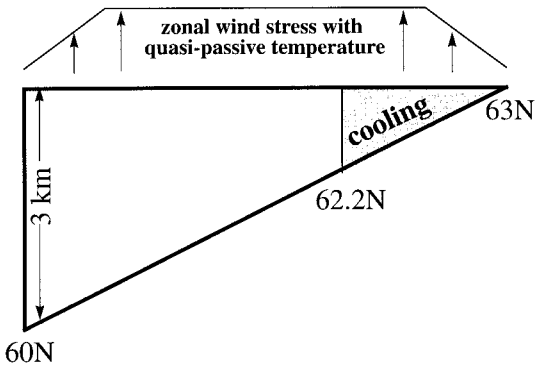

FIG. 5. Schematic representation of the two-dimensional experiments of sections four and five. The basin is a re-entrant channel in the *x* direction with a uniform slope of slightly less than 0.01 in the *y* direction. In the first series of experiments (Fig. 6), a quasi-passive tracer flows downslope under the influence of downwelling favorable (westward) wind stress. In the second series of experiments (Fig. 8), no wind stress is applied and stronger density anomalies advect themselves down the slope.

ary layers are found adjacent to the bottom. Figure 3a is overprinted with the temperatures of all of the 70-m thick grid boxes at 2.6°E. The bottom seven temperatures are identical indicating a convectively mixed layer 490-m thick. As dense fluid moves offshore in the *z* model it mixes convectively with the lighter water below. This process accounts for the rapid offshore reduction of density in Fig. 2a.

Figure 4 shows the barotropic streamfunction for the two models at the end of the first year. The sinking of dense water to depth in the ρ model induces a strong anticyclonic flow centered over the deepest part of the basin. From a vorticity perspective, this is due to the compression of light fluid by the dense fluid filling in at the bottom and is related to the hypsometric effect of Rhines and MacCready (1989). In the *z* model, the volume flux of the anticyclonic flow is lower by more than an order of magnitude.

In many respects the solutions found by the two models are opposite. In the ρ model, dense water flows out from the northern shelf and sinks vigorously, converting potential to kinetic energy, developing an energetic anticyclonic flow. The *z* model exhibits only weak sinking of dense fluid and, as a result, develops much less flow. The contrast is striking in view of our having performed, as nearly as practical, the same experiment with two different implementations of the primitive equations. For some resolution the solutions must approach convergence. Our purpose in the remainder of the paper is to find the resolution required for this and to develop a theoretical framework to ensure that the models converge to the correct solution. Toward this end we revert to two-dimensional experiments in the next two sections. The next section addresses the convective entrainment problem specifically and the following section demonstrates convergence of the models to a theoretical estimate of the frictional sinking rate.

4. Downslope flow over *z*-coordinate steps

To explore very high resolution in the *z* model and to compare to theoretical ideas (developed in the next section), we employ a two-dimensional configuration of both the *z* and ρ models in the rest of the paper. Our basin for these explorations will be an *f*-plane channel, re-entrant in the *x* direction, 3° in meridional extent, with a linearly sloping bottom 3-km deep at the southern boundary (Fig. 5).

We noted in the last section that thick bottom mixed

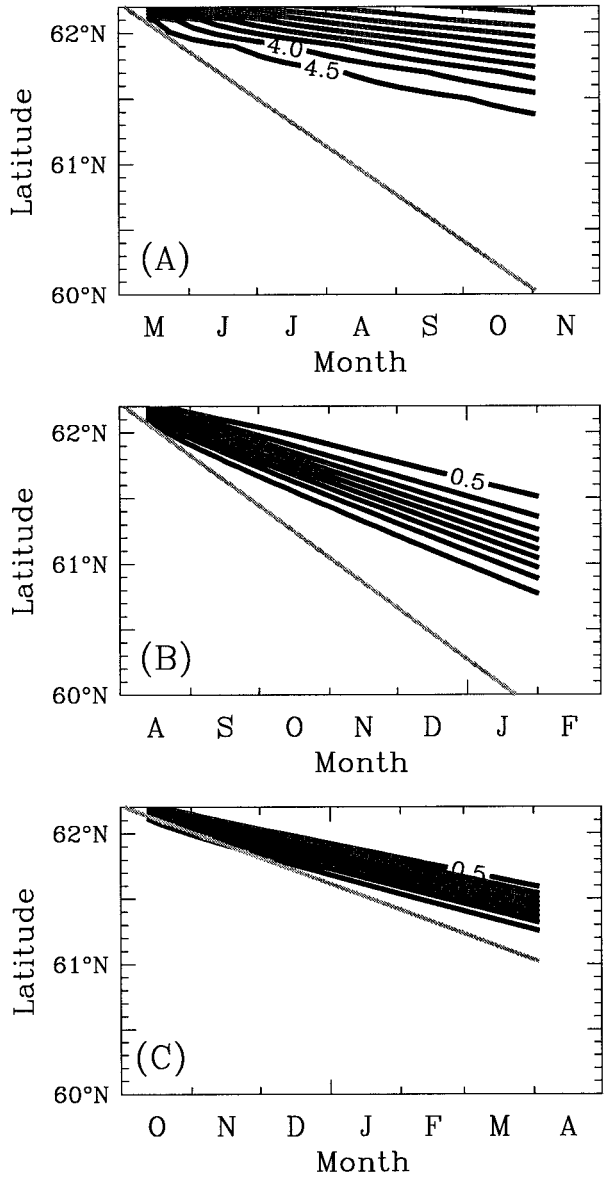

FIG. 6. The evolution at the bottom of a quasi-passive tracer driven downslope by downwelling favorable wind stress. Three *z*-model experiments are shown: (a) $\Delta z = 50$ m, $\Delta y = 0.2°$; (b) $\Delta z = 50$ m, $\Delta y = 0.05°$; and (c) same resolution as (b) but $A = 0.5$ m^2 s^{-1}. (a) and (b) Identical experiments except that (b) has sufficient horizontal resolution to resolve the slope ($\Delta x \approx \Delta z/\alpha$). (c) Marginally resolves the bottom viscous layer in addition to the slope.

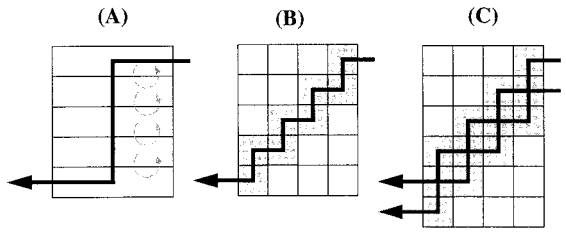

FIG. 7. Schematic representation of the reduction in convective entrainment that accompanies improved resolution. When the horizontal resolution does not resolve the slope, the dense signal in the bottom layer mixes with a column of ambient fluid $\alpha(\Delta x/\Delta z)$ times as thick at every step (a). With slope-resolving horizontal resolution, the ratio of dense signal to light ambient fluid mixed at the steps rises to one-to-one (b). When the viscous layer is also resolved, the ratio rises above one-to-one (c).

layers developed in the *z*-coordinate simulation. The density of these layers was reduced in the offshore direction. In the *z* model, offshore dense water flows induce convection when crossing steps. The mixing with ambient water that results depletes the initial density signal. To isolate this convective entrainment effect from its dynamical ramifications and to examine its sensitivity to resolution we shall first perform *z*-model experiments in the two-dimensional channel basin driven primarily by westward (downwelling favorable) wind stress.

This wind forcing induces a downslope flow along the bottom with the compensating return flow occurring near the surface. The wind-driven flow advects a quasi-passive tracer (temperature) forced by cooling in the shallow region. The associated density anomaly is made a factor of 100 smaller than that used elsewhere in this paper by reducing the thermal expansion coefficient by a factor of 100 from the standard 0.2 kg (m^3 °C)$^{-1}$. This density anomaly (0.01 kg m^{-3}) is sufficient to induce convective entrainment as it moves offshore but does not significantly affect its own advection. A uniform westward wind stress of 0.1 Pa is applied over the central 2° of the basin and tapered linearly to zero at the boundaries. These boundary regions contain the vertical sections of the induced flow. The water north of 62.2°N (where the depth is 800 m) is continually cooled toward the full anomaly with a 5-day timescale. Shortly, we will present a similar set of experiments but without wind stress and with the large thermal expansion coefficient to show that the results of these ''quasi-passive'' experiments also apply to the case where the dense water is self-advecting.

Three experiments have been performed all having the same vertical grid size, 50 m. The first has the same horizontal resolution as the *z*-grid model used in the last section—0.2° lat. The second experiment is identical to the first but with the horizontal resolution refined by a factor of 4. The third experiment employs this higher resolution and also has a vertical viscosity that is 25 times larger (0.5 m^2 s^{-1}) than that used in the previous two experiments. The Ekman layer thickness, $\sqrt{2A/f}$, is thereby increased from about 20 m to about 100 m making the third experiment marginally Ekman layer resolving.

Of interest are the dispersion and propagation errors in the movement of the bottom front. The actual bottom front is compared with the motion of an ideal front moving with the bottom flow for each of the three experiments in Fig. 6. The front in the low horizontal

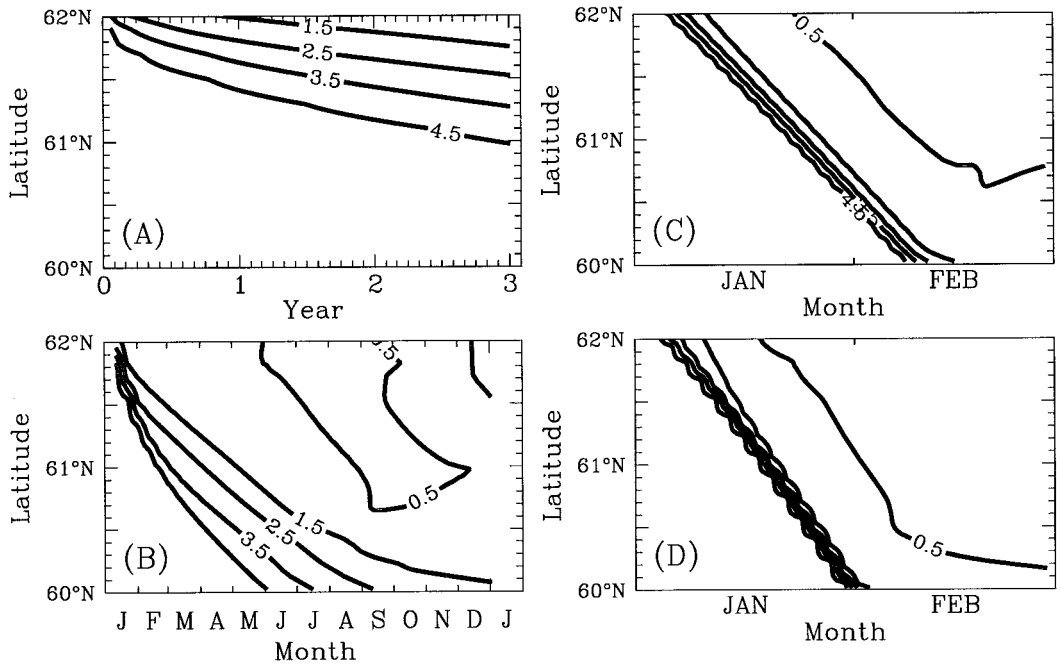

FIG. 8. Evolution at the bottom of a self-advecting cold anomaly in four *z*-model experiments: (a) $\Delta z = 50$ m, $\Delta y = 0.2°$; (b) $\Delta z = 50$ m, $\Delta y = 0.05°$; (c) same resolution as (b) but $A = 0.5$ m^2 s^{-1}; and (d) same viscosity as (c) but slightly higher resolution ($\Delta z = 30$ m, $\Delta y = 0.03°$).

resolution case (Fig. 6a) rapidly loses sharpness and lags far behind its expected location. These features are the result of strong convective entrainment. A closer inspection of the solution shows that, although the downslope flow is confined to the bottom 50 m, it is contained within a convectively mixed layer 250 m thick. In this case the vertical resolution is misleading because, when moving one horizontal grid point offshore, the flow descends (and convectively mixes with) four vertical grid points (Fig. 7a). This suggests that the solution may be improved by refining the horizontal grid so that it resolves the slope (Fig. 7b), that is, by setting $\Delta x = \Delta z/\alpha$ where α is the slope. This has been done in the second experiment, and Fig. 6b shows the improvement in the sharpness and propagation of the front.

We might expect that as the grid is further refined horizontally and vertically to resolve the viscous boundary layer (Fig. 7c), convective entrainment will be further reduced and the movement and maintenance of the front will become more accurate. Even in a two-dimensional model, the necessary resolution becomes cumbersome, so we investigate this effect by increasing the vertical viscosity, making the Ekman layer thick enough to be resolved. Figure 6c shows that, when this is done, there is a further improvment in frontal sharpness and propagation.

The propagation error due to convective mixing can be understood in terms of the relative heights of the flow and the convectively mixed layers. The true velocity of the front is the signal containing volume flux divided by the height of the signal containing volume. For a given viscous layer velocity this is proportional to the viscous layer height divided by the convective layer height. These ratios are 1:5, 1:2, and 2:3 for the grids used in the experiments of Figs. 6a–c (see Fig. 7). The ratios of actual front speed to viscous layer flow speed for the three experiments determined from Fig. 6 are close to these expected values. In Fig. 7, the slope-resolving grid (Fig. 7b) and the slope- and flow- resolving grid (Fig. 7c) are shown embedded in the coarse resolution grid to illustrate the importance of the grid refinements for reducing the flow height/convective mixed-layer height ratio. In addition to the propagation error, Fig. 6 shows resolution-dependent dispersion of the front. The frontal spreading appears to be linear and to scale with the propagation speed error.

Now we repeat the experiments but without wind stress and with a fully active temperature tracer in order to determine if the conclusions regarding the dependence of the bottom front simulation upon resolution carry over to the case where the front is self-advecting. For these experiments the triangular cooling region depicted in Fig. 5 is restored to a density 1 kg m^{-3} greater than that of the ambient water on a 5-day timescale.

Figure 8 shows Hovmöller plots of bottom temperature for four of these density-forced experiments. The first three experiments (Figs. 8a–c) correspond to those of Figs. 6a–c. The fourth (Fig. 8d) is a slightly higher resolution version of the third. In the low horizontal resolution case (Fig. 8a), the bottom temperature signal is greatly diffused over the course of three years. The leading edge reaches only about 1500-m depth by the

end of this period. When the slope is resolved horizontally (Fig. 8b), the bottom temperature front is still considerably diffused but it reaches 3000 m after about six months. This is much larger than the corresponding time for a comparable ρ-model experiment in which the front reached the bottom in about 8 days. As in the last section, we resolve the bottom viscous layer by increasing the vertical viscosity from the $A = 0.02$ m^2 s^{-1} used in Figs. 8a and 8b to $A = 0.5$ m^2 s^{-1} in Figs. 8c and 8d. The experiment of Fig. 8c has nearly 2 grid points in an Ekman layer thickness, whereas that of Fig. 8d has nearly 3. Both experiments have slope-resolving horizontal resolution. The bottom temperature front reaches 3000-m depth much more rapidly in these experiments—in about one month. Neither experiment shows the diffusive spreading of the front seen in the non-Ekman layer resolving experiments. In Fig. 8d, the front actually tightens as colder water overtakes warmer during the descent (the colder water is the product of more thorough cooling after the 5-day cooling timescale has elapsed). With our linear friction, the downslope flow scales as the alongslope flow. Assuming a resting upper layer, the alongslope geostrophic flow in the lower layer is $g'\alpha/f$, where the interface parallels the slope (g' is the reduced gravity). From this simple idealization of the flow we expect cold water to overtake warmer.

The front in Fig. 8d propagates at 9 cm s^{-1}, whereas the downslope flow speed slightly behind the front is 16 cm s^{-1}. We attribute this discrepancy to remaining convective entrainment. The cold water in a similarly configured ρ model reaches the bottom in 10 days, propagating at 28 cm s^{-1}, slightly faster than the downslope flow speed of 25 cm s^{-1} slightly behind the front. The increased resolution used in the Fig. 8d experiment has increased the propagation of the front by more than 25%. We expect that further refinement of the resolution would yield further increases in frontal propagation speed.

5. Convergence of the models to a theoretical sinking rate

In the previous section we demonstrated that a slope- and viscous-layer-resolving grid is necessary to allow realistic dense water sinking in the z model. One might well wonder, however, what the correct sinking rate is for our modeled setting and if the z model becomes quantitatively correct once the requisite resolution is employed. To address these questions, we develop an analytical estimate of the sinking rate for the two-dimensional problem depicted in Fig. 5 and compare the sinking rates of the z and ρ models to it. The reader who is uninterested in these details may proceed directly to the conclusions.

It will prove conceptually useful to partition the frictional flow into a part driven by bottom stress and a part driven by frictional stress at the interface between dense and light water. Bottom-stress-driven two-dimensional flows have been treated analytically by MacCready (1994) and Condie (1995). Both of these studies assume a resting upper layer, however, while motion in this layer plays a key role in the current experiments. In these experiments, the downslope flow driven by bottom stress is balanced by upslope flow in the upper layer. The Coriolis force provides eastward acceleration of this layer. Since the interface tends to parallel the slope, the geostrophic velocity difference can be approximated by

$$U_s = g'\alpha/f. \tag{3}$$

When the upper-layer geostrophic flow becomes equal to U_s, the pressure gradient at the bottom no longer favors downslope frictional flow and the bottom-drag-driven overturning shuts down. Rhines and MacCready (1989) describe a similar shutdown phenomenon where the unfavorable pressure gradient develops as a result of buoyancy advection in the Ekman layer itself. We can estimate the downslope volume flux that will occur before shutdown of the bottom-stress-driven flow. The argument is based upon following a line of fluid as it ascends the slope in the upper layer (Fig. 9). The Lagrangian form of the u-momentum equation,

$$\frac{Du}{Dt} = fv = f\frac{Dr}{Dt}, \tag{4}$$

is integrated (assuming the line of fluid is initially at rest) to give

$$u = fr. \tag{5}$$

Applying the shutdown condition $u = U_s$ gives [using Eqs. (3) and (5)]

$$r = g'\alpha/f^2. \tag{6}$$

The volume of fluid that must pass a point with depth H_0 (in both directions) in order for this condition to be met is then

$$V = r(H_0 + \alpha r/2) = \frac{g'\alpha}{f^2}\left(H_0 + \frac{g'\alpha^2}{2f^2}\right) \approx \frac{\alpha g' H_0}{f^2}. \tag{7}$$

The precise bottom friction formulation and the magnitude of frictional parameters do not affect the downslope volume flux preceding shutdown. These will, however, affect the shutdown timescale with greater friction leading to more rapid shutdown.

From (7) it is clear that the most stringent shutdown condition will be enforced where the depth H_0 is small. However, adjacent to the forcing region, the slope of the interface exceeds the slope of the bottom, locally invalidating an assumption used in deriving (7). This ambiguity prevents us from establishing a firm estimate based upon parameters chosen prior to the experiment. The volume flux of dense fluid south of midbasin ($y = 61.5°$N) is plotted as a function of time in Fig. 10 for several experiments. The ''ρ-model-1'' experiment is the standard ρ model with vertical viscosity and horizontal resolution chosen to match the z-model experi-

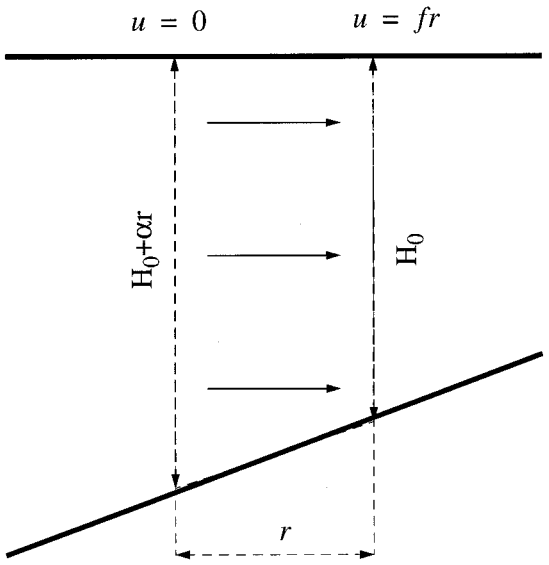

FIG. 9. Schematic representation of estimation of dense water sinking in a bottom stress driven flow.

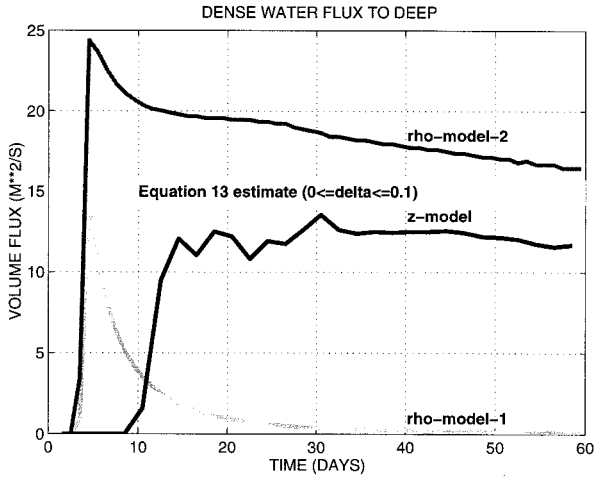

FIG. 10. Volume flux of dense water south of 61.5°N (below 1500 m). For the z-model "dense" is defined as colder than 2.5°C. The z-model result can be compared to the ρ-model-2 result and the lower edge of the Eq. (13) estimate. The ρ-model-1 curve demonstrates shutdown of the bottom drag–driven flow in a model with a nearly inviscid upper layer.

ments depicted in Figs. 8c and 8d. Because of the upper layer's large thickness, it is nearly inviscid. Shutdown is indicated in Fig. 10 for this experiment by the approach of the volume flux to zero. The total volume of fluid to pass $y = 61.5°$N after 60 days matches the estimate [Eq. (7)] with $H_0 = 1200$ m. This is midway between the maximum depth in the forcing region (800 m) and the point where the slope of the interface first exceeds the bottom slope (1600 m).

The dense water volume flux for the highest resolution z model (corresponding to Fig. 8d) is also plotted in Fig. 10. This case does not approach zero as in the ρ-model-1 experiment because, in this experiment, there is an overturning driven by viscous shear at the dense/light interface in addition to the one driven by bottom stress. Figure 11a shows that both the downslope and upslope portions of this flow are contained in the region where the zonal flow is significantly affected by viscous effects—the maximum u occurs above the upslope/downslope couple. The upslope flow, like the downslope, is the result of frictional crossing toward low pressure.

To verify the structure of the z-model solution and its rate of sinking, we model the combined bottom and interfacial frictional layers by solving the Ekman layer equation for a configuration having a discontinuous jump in geostrophic flow from $U_0 - U_s$ to U_0 a distance h above the bottom. Here U_s represents the jump in geostrophic velocity of $g'\alpha/f$ at the plume top and U_0 the geostrophic flow well above the plume. The Ekman layer equation is

$$if(\tilde{u} - U_0 + \mathcal{H}(-z)U_s) = K\frac{\partial^2\tilde{u}}{\partial z^2}, \tag{8}$$

where $\tilde{u} = u + iv$ is the complex horizontal velocity, and $\mathcal{H}$ is the Heaviside step function. It is convenient to locate the interface at $z = 0$ and the bottom at $z = -h$. The boundary conditions are then: $\tilde{u}(-h) = 0$ and $\tilde{u} \to U_0$ as $z \to \infty$. We find separate solutions above and below $z = 0$ and match them and their first derivatives there, giving

$$\tilde{u} = \begin{cases} \dfrac{U_s}{2}\exp\left(\dfrac{(1+i)z}{\sqrt{2A/f}}\right) + \gamma\exp\left(\dfrac{-(1+i)z}{\sqrt{2A/f}}\right) + U_0 - U_s & \text{for } z < 0 \\ \left(\gamma - \dfrac{U_s}{2}\right)\exp\left(\dfrac{-(1+i)z}{\sqrt{2A/f}}\right) + U_0 & \text{for } z \geq 0, \end{cases} \tag{9}$$

where

$$\gamma = \exp\left(\frac{-(1+i)h}{\sqrt{2A/f}}\right) \times \left\{\left[1 - \frac{1}{2}\exp\left(\frac{-(1+i)h}{\sqrt{2A/f}}\right)\right]U_s - U_0\right\}. \tag{10}$$

An Ekman layer solution is shown next to that of the z model in Fig. 11b. The Ekman model has three parameters: U_s, h, and U_0. Here U_s is determined a priori while U_0 and h are set to match the z-model upper-layer flow and depth of the dense water layer. Both Ekman and z-model solutions show an upslope flowing layer over a downslope flowing one and have a small overshoot in u above the maximum upslope flow. The main

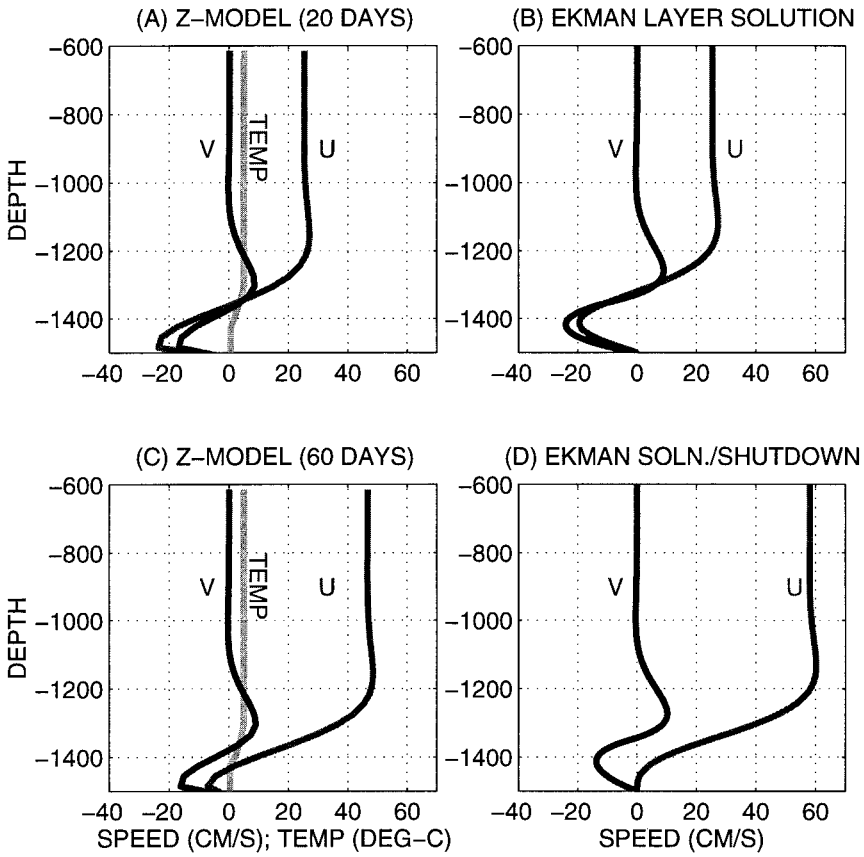

FIG. 11. (left) Bottom-layer structure for the highest resolution z model at 61.5°N at 20 days (a) and 60 days (c). (right) Triple Ekman layer solution using $h = 150$ m, $U_s = 70$ cm s^{-1}, and $U_0 = 25.4$ cm s^{-1} (b) and with U_0 determined by the condition of no stress at the bottom (d). The estimate of the dense water sinking rate shown in Fig. 10 is based upon the Ekman layer depicted in (d) where shut down of the bottom stress–driven flow has been assumed.

difference is that the downslope flow is stronger than the upslope flow in the Ekman model case. This model does not have momentum equation terms that would allow it to balance the upslope and downslope flow while maintaining a nonzero stress at the bottom.

While the z-integrated cross-slope flow driven by interfacial stress is zero, the bottom stress–driven flow is balanced by opposite flow, predominantly in the inviscid portion of the upper layer. As discussed earlier, this leads to shutdown of the bottom stress–driven flow. Figure 11c shows the z-model solution after it has progressed significantly toward this state. We can solve the Ekman model for the zero bottom stress state by setting

$$\frac{\partial u}{\partial z} = 0 \tag{11}$$

at $z = -h$. This fixes U_0 in terms of U_s and h:

$$U_0 = U_s\left\{1 - \exp\left(\frac{-h}{\sqrt{2A/f}}\right) \times \left[\cos\left(\frac{-h}{\sqrt{2A/f}}\right) + \sin\left(\frac{-h}{\sqrt{2A/f}}\right)\right]\right\}. \tag{12}$$

The integrated downslope (or upslope) flow within the layers from Eq. (9) is, then

$$-\int_{-h}^{0} v\, dz = \int_{0}^{\infty} v\, dz = \frac{U_s}{2}\sqrt{\frac{A}{2f}}(1 - \delta), \tag{13}$$

where

$$\delta = \exp\left(\frac{-2h}{\sqrt{2A/f}}\right)\left\{1 + 2\sin\left(\frac{h}{\sqrt{2A/f}}\right)\left[\cos\left(\frac{h}{\sqrt{2A/f}}\right) + \sin\left(\frac{h}{\sqrt{2A/f}}\right)\right]\right\}. \tag{14}$$

The Ekman solution for this case is shown in Fig. 11d. This can be compared with the *z*-model solution after 60 days (Fig. 11c). Here U_s and h are as in Fig. 11b but U_0 is now determined by Eq. (12). Both solutions show u is small relative to v in the dense water. The Ekman solution U_0 is somewhat larger, primarily because the geostrophic shear in the *z*-model density structure is about 90% of U_s. The rate of downslope dense water flux as estimated from Eq. (13) is 14 m^2 s^{-1}, whereas the *z*-model flux is 12 m^2 s^{-1} near the end of the first 60 days (Fig. 10). The agreement with the Ekman model is reasonably good. The δ term in Eq. (13) is not negligible in the *z*-model volume flux estimate, giving a reduction of about 10%.

Now we demonstrate that the ρ model also gives a sinking rate consistent with the theoretical estimate. A small modification to the ρ model is necessary in order to do this. The ρ model, by construction, is incapable of representing shears within constant density layers such as are seen in the *z*-model solution (Figs. 11a and 11c). Thus, in addition to the standard ρ model (ρ model 1), we have configured a second version (ρ model 2) with interfacial stress calculated based upon the minimum of the Ekman layer thickness and the layer thickness, similar to the parameterization of bottom stress. Figure 10 also shows the volume flux for this experiment. The volume flux rate at the end of 60 days is about 17 m^2 s^{-1}. This is quite comparable to the estimate of 16 m^2 s^{-1} from Eq. (13) when the δ term is neglected. The bottom layer is so thick in the ρ-model-2 experiment that the δ effect is not significant.

6. Conclusions

In this paper we have investigated the potential for explicitly simulating density-driven frictional sinking along slopes in *z*-coordinate models. This process is thought to be the primary mechanism for replenishing deep water in the natural ocean. The convective entrainment that occurs when dense water flows out from a step over lighter ambient water was found to be a major impediment to proper simulation of the flow. Even for resolution comparable to that used by current eddy-permitting simulations, this entrainment prohibits significant frictional sinking. A density-coordinate model that does not have convective entrainment predicts a much greater rate of dense-water sinking.

The errors due to convective entrainment were shown to be truncation errors in the sense that they are reduced by increasing the grid resolution. The resolution needed to significantly overcome the convective entrainment problem was determined from experiments with a two-dimensional model. This model gave results consistent with theory and the density coordinate model solution when 1) the horizontal resolution was slope resolving (i.e., $\Delta x \approx \Delta z/\alpha$, where α is the slope) and 2) the vertical grid spacing resolved several points within the bottom frictional layer.

Since a typical vertical scale for the overflow plumes is 100 m and a typical slope is 0.01, these conditions imply that resolution on the order of 30–50 m in the vertical and 3–5 km in the horizontal will be needed to represent frictional sinking with reasonable accuracy. This resolution is prohibitive for climate simulations, which require thousands of years to establish a balance between downward advection of cold water and diffusion of heat. Our results therefore suggest that parameterization of frictional sinking will be required in these models in order to produce realistic deep-water properties via the appropriate mechanism. Beckman and Doscher (1997) have proposed a parameterization that averts convective events by rearranging mass flow at the bottom. They show an example where this improves sinking of a dense plume. Another approach is to model the frictional bottom boundary layer on a separate two-dimensional grid (Gnanadesikan et al. 1998, submitted to *J. Phys. Oceanogr.*). This approach offers the added flexibility to use finer vertical resolution adjacent to the bottom than elsewhere at a given level, and to calculate the pressure gradient in a bottom-following coordinate system.

The results of this paper may have implications for climate model sensitivity as well as for biases in equilibrium states. The large difference in the response of the models in the section 3 experiment suggests that the *z*-coordinate models may underestimate the ocean response to climate perturbations, although it should be borne in mind that the initial condition was climatically unrealistic and entrainment was neglected. Further investigations with more realistic parameters will be needed to assess the role of frictional sinking in ocean sensitivity to climate change.

Acknowledgments. The authors thank Ron Pacanowski for assistance using the MOM 2 code. Robbie Toggweiler and two anonymous referees are thanked for carefully reviewing a preliminary version of the manuscript. Jerry Mahlman and Steve Griffies also made helpful comments. RH was supported by a UCAR Ocean Modelling Postdoctoral Fellowship and a Visiting Scientist Fellowship from Princeton University.

REFERENCES

Beckman, A., and R. Doscher, 1997: A method for improved representation of dense water spreading over topography in geopotential-coordinate models. *J. Phys. Oceanogr.,* **27,** 581–591.

Bleck, R., and L. T. Smith, 1990: A wind-driven isopycnic coordinate model of the North and Equatorial Atlantic Ocean. Part 1: Model development and supporting experiments. *J. Geophys. Res.,* **95,** 3273–3285.

Condie, S. A., 1995: Descent of dense water masses along continental slopes. *J. Mar. Res.,* **53,** 897–928.

Danabasoglu, G., J. C. McWilliams, and P. R. Gent, 1994: The role of mesoscale tracer transports in the global ocean circulation. *Science,* **264,** 1123–1126.

Gerdes, R., and C. Koberle, 1995: On the influence of DSOW in a

numerical model of the North Atlantic general circulation. *J. Phys. Oceanogr.*, **25,** 2624–2642.

Gnanadesikan, A., M. Winton, and R. Hallberg 1998: Representing the bottom boundary layer in the GFDL ocean model: Model framework, dynamical impacts and parameter sensitivity. *J. Phys. Oceanogr.*, **28,** in press.

Hallberg, R., 1995: Some aspects of the circulation in ocean basins with isopycnals intersecting topography. Ph.D. dissertation, University of Washington, 244 pp. [Available from University Microfilms, 1490 Eisenhower Place, P.O. Box 975, Ann Arbor, MI 48106.]

——, 1997: Stable split time stepping schemes for large-scale ocean modeling. *J. Comput. Phys.*, **135,** 54–65.

Hirst, A. C., and T. J. McDougall, 1996: Deep-water properties and surface buoyancy flux simulated by a z-coordinate model including eddy-induced advection. *J. Phys. Oceanogr.*, **26,** 1320–1343.

MacCready, P., 1994: Frictional decay of abyssal boundary currents. *J. Mar. Res.*, **52,** 197–217.

Pacanowski, R. C., 1995: *MOM 2 Documentation, User's Guide and Reference Manual*. GFDL Ocean Tech. Rep. No. 3, 232 pp. [Available from NOAA/GFDL, Princeton, NJ 08542.]

Price, J. F., and M. O. Baringer, 1994: Outflows and deep water production by marginal seas. *Progress in Oceanography*, Vol. 33, Pergamon, 161–200.

Rhines, P. B., and P. MacCready, 1989: Boundary control over the large scale circulation. *Proc. Fifth 'Aha Huliko'a Hawaiian Winter Workshop*, Honolulu, HI, Hawaii Institute for Geophysics, 75–97.

Toggweiler, J. R., 1994: The ocean's overturning circulation. *Phys. Today*, **47,** 45–50.